Journal of Membrane Science 618 (2021) 118736

Contents lists available at ScienceDirect

Journal of Membrane Science

journal homepage: http://www.elsevier.com/locate/memsci

The effects of sulphur poisoning on the microstructure, composition and oxygen transport properties of perovskite membranes coated with nanoscale alumina layers

Guangru Zhang [a,e], Dragos Neagu [b,e], Peter J. King [c,e], Sami Ramadan [d,e], Anthony O'Neill [e], Ian S. Metcalfe [e,*]

[a] State Key Laboratory of Materials-Oriented Chemical Engineering, College of Chemical Engineering, Nanjing Tech University, China
[b] Department of Chemical and Process Engineering, University of Strathclyde, UK
[c] Picosun Group, Finland
[d] Department of Materials, Imperial College London, UK
[e] School of Engineering, Newcastle University, UK

ARTICLE INFO

Keywords:
Perovskite membranes
Atomic layer deposition
Oxygen permeation
H_2S poisoning
Interfaces

ABSTRACT

Perovskite oxides displaying mixed ionic and electronic conductivity have attracted a lot of interest for application in oxygen separation membranes. Such membranes could be used for a range of processes, including the conversion of natural gas to hydrogen or syngas. A major limitation of these materials is their tendency to segregate into simpler oxides under operating conditions, reacting with sulphur-based species often found in natural gas and leading to irreversible membrane degradation over time. Here we aim to delay or prevent this process by coating $La_{0.6}Sr_{0.4}Co_{0.2}Fe_{0.8}O_{3-\delta}$ membranes with Alumina (Al_2O_3) layers of 1–100 nm thickness by using atomic layer deposition. We show that coatings of about 30 nm have negligible negative effect on O_2 transport flux across the membrane and display good flux recovery when H_2S is removed from the stream. Coatings thinner than this critical value provide little protection against irreversible poisoning while thicker coatings dramatically decrease overall O_2 permeation fluxes. We also show that the irreversible sulphur poisoning under O_2 permeation conditions is linked to microstructural and composition changes at the membrane surface caused predominantly by the formation of $SrSO_4$ particles at the perovskite grain boundaries.

1. Introduction

Perovskite oxides (ABO_3) exhibiting mixed ionic and electronic transport properties such as $La_{1-x}Sr_xCo_{1-y}Fe_yO_{3-\delta}$ have received increased attention for application in oxygen separation membranes [1]. Among other applications, such membranes could be used for the selective conversion of natural gas (primarily methane) to hydrogen or syngas [2,3]. However, these perovskites are known to segregate ions from the A- and B-sites, particularly under O_2 permeation conditions, which can react with sulphur-based species often found in natural gas, leading to irreversible membrane degradation over time [3–7]. Similar limitations are also observed when these materials are applied in the related area of solid oxide cell electrodes [4,8,9].

One approach to limiting degradation could be by coating the membranes with a protective layer that would limit oxide segregation and potential follow-up reactions. A method that allows the coating of supports with continuous, conformal layers of controlled thickness is atomic layer deposition (ALD, Fig. S1). Moreover, ALD is becoming increasingly more applicable at a larger, batch scale [10]. One material that could prevent degradation due to its relatively low chemical reactivity and which is routinely used in ALD processes is Al_2O_3. While this is expected to provide some protection against degradation, it is also expected to lower O_2 transport since the oxygen diffusion in Al_2O_3 is between 5–10 orders of magnitude lower than in perovskites (large variations observed depending on doping and microstructure) [11,12]. Nonetheless, if sufficiently thin coatings are applied, such that the oxygen diffusion coefficient of the phases normalized to their respective thickness is of similar order of magnitude, e.g. 100 nm or less, the compromise in O_2 permeation could be acceptable.

Here we prepare $La_{0.6}Sr_{0.4}Co_{0.2}Fe_{0.8}O_{3-\delta}$ (LSCF) membranes coated

* Corresponding author.
E-mail address: ian.metcalfe@ncl.ac.uk (I.S. Metcalfe).

https://doi.org/10.1016/j.memsci.2020.118736
Received 26 May 2020; Received in revised form 4 September 2020; Accepted 7 September 2020
Available online 11 September 2020

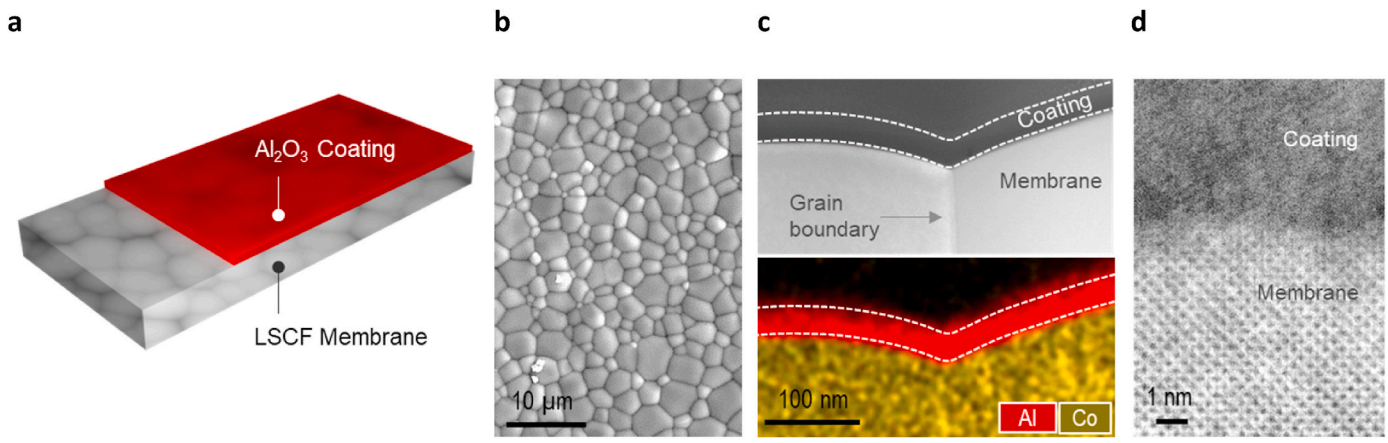

Fig. 1. Microstructure of the coated membranes. (a) schematic representation of the LSCF membranes coated with Al_2O_3 layers by ALD. **(b)** SEM micrograph of the surface of an uncoated membrane. **(c)** TEM micrograph of the membrane-coating interface and corresponding elemental map (for Al and Co) by EDX analysis (see Fig. S4 for all other elements). **(d)** TEM micrograph of the membrane-coating interface.

with 1–100 nm Al_2O_3 layers and study the effect of H_2S poisoning on their microstructure, composition and oxygen transport properties. We show that coatings of up to 30 nm have negligible negative effect on O_2 transport flux across the membrane and display good flux recovery when H_2S is removed from the stream. Thinner coatings provide little protection against irreversible poisoning while thicker coatings dramatically decrease overall O_2 permeation fluxes. We also show that the irreversible sulphur poisoning under O_2 permeation conditions is linked to microstructural and composition changes at the membrane surface caused predominantly by the formation of $SrSO_4$ particles at the perovskite grain boundaries.

2. Experimental

2.1. Coating preparation

Membranes consisting of dense LSCF (~1.2 mm thickness) were coated with Al_2O_3 layers of various thickness by ALD by using an Oxford Instruments Flex Al reactor. A planar Si chip was also coated for thickness reference measurements. The deposition temperature was set at 200 °C, while the base pressure of the reactor was 2×10^{-6} Torr, with the chamber pressure being held at 0.08 Torr during deposition. The pulse/purge times were 0.02/1.5 s for trimethyl aluminium (TMA) and 0.04/6 s for H_2O.

2.2. X-ray diffraction

XRD was carried out on the coated membranes (Fig. S2), on a PANalytical X'Pert Pro diffractometer (PW3040/60) fitted with an X'Celerator and a secondary monochromator. For data acquisition, the Cu anode was supplied with 40 kV and a current of 40 mA to generate Cu Kα ($\lambda = 1.54180$ Å) or Cu $K_{\alpha 1}$ ($\lambda = 1.54060$ Å) radiation.

2.3. Raman spectroscopy

Raman spectra were collected using a Horiba Yvon LabRam HR system equipped with a 514.5 nm laser. An exposure time of 10 s, 100X objective lens and 2400 gr/mm grating were used.

2.4. Scanning electron microscopy

SEM micrographs were recorded on a Tescan Vega 3LMU scanning electron microscope. To reduce charging effects, the samples were sputtered with thin film of gold.

2.5. Cross-section transmission electron microscopy

Focused ion beam (FIB) was employed to extract a cross-section lamella from the coating-membrane interface. This was carried out using a FEI Scios Dualbeam instrument. The sites of interest were protected from the gallium ion beam by locally depositing a carbon layer followed by the application of a thicker platinum layer. Gallium ion beam was then used to carve out a lamella, which was then mounted on a TEM grid and ion milled until electron transparent. TEM and scanning transmission electron microscopy (STEM) were carried out using a FEI Titan Themis S/TEM operated at 200 kV equipped with a Super-X windowless X-ray energy dispersive spectrometer (EDS).

2.6. O_2 permeation experimental setup

The setup used to carry out the O_2 permeation experiments is schematically illustrated in Fig. S5. The supply of various gases, Ar (C1), 200 ppm H_2S in Ar (C2), and synthetic air (21% O_2 in N_2) (C3) was controlled by mass flow controllers (Brooks, SLA5850) and set to 30 cm^3 (STP) min^{-1} for each individual gas stream. These gasses were fed to the reactor consisting of an Al_2O_3 tube. The pellet membrane was mounted on top of the Al_2O_3 tube using a high temperature commercial silver sealant (Fuel Cell Materials, AG-I). The gas composition at the permeate side outlet was determined by using a gas chromatographer (Varian-3800) equipped with 5A molecule sieve column with a sampling rate of 2 h/injection.

2.7. Residence time distribution

The volumes of the feed and permeate side chambers are 14 and 157 cm^3, respectively. A pules tracer, containing 2 mL air, was introduced into the system at the inlet. The concentration of the tracer (oxygen) at the outlet was monitored by a mass spectrometer (GeneSys). As shown in Fig. S6, the residence time distribution (RTD) for the permeate side indicated that it was very close to a continuous flow stirred tank reactor (CSTR) while the feed side was close to a plug flow reactor (PFR). Therefore, the permeate side membrane surface would be exposed to not only the hydrogen sulfide but also oxidation products such as SO_2.

2.8. O_2 permeation measurement

Permeation experiments were conducted at a temperature of 900 °C, generally in three stages. In all stages, the feed side of the membrane was exposed to a flow synthetic air (21% O_2, 79% N_2), while the permeate side (where the coating would be present) was exposed to a flow of Ar

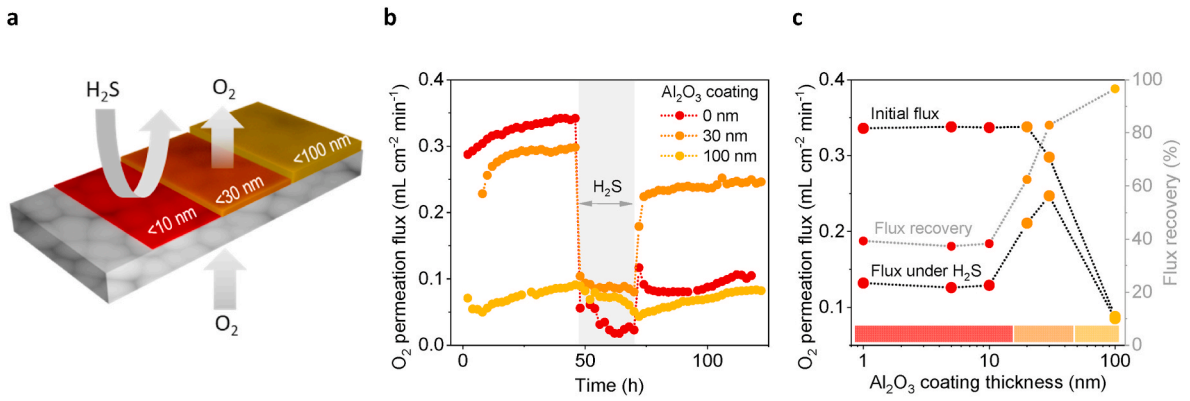

Fig. 2. The effect of coating thickness on O_2 permeation under H_2S. (a) schematic representation of membranes with various coating thickness employed in O_2 permeation experiments. **(b)** O_2 permeation flux as a function of time, before, during and after exposure to H_2S, for membranes with different coating thickness. **(c)** O_2 permeation flux before and after exposure to H_2S, as well as flux recovery, as a function of coating thickness (on logarithmic scale). The dotted lines serve as guide to the eye.

(stage I), 200 ppm H_2S in Ar (stage II) and then Ar (stage III). Permeation experiments for each coating thickness were repeated at least three times to ensure repeatability. The leakage of the oxygen that might occur due to imperfect sealing at high temperatures was monitored through the mole fraction of N_2 (79 mol/% in the feed side) leaked into the permeate side. Experiments were only considered if the leakage of N_2 was below 0.5 mol.%. The oxygen permeation flux was calculated by:

$$J_{O_2} = \frac{\left(C_{O_2,\,outlet} - \frac{0.21}{0.79}C_{N_2,outlet}\right)\cdot Q_{inlet}}{S}$$

Where $C_{O_2,\,outlet}$ and $C_{N_2,outlet}$ are the O_2 and N_2 mole fraction at the permeate side outlet, respectively, Q_{inlet} is the gas flow rate in the permeate side inlet and S is the effective membrane area.

Selectivity is impossible to determine since leak rates may be higher than non-selective permeation. Additionally, there was no evidence that leak rates increased with exposure to poisons.

3. Results and discussion

3.1. Microstructure of the coated membranes

A schematic representation of the coated membranes developed and used in this study is shown in Fig. 1a. The membranes were prepared in the form of dense pellets, consisting of LSCF perovskite with a polycrystalline microstructure (1–5 μm diameter grains), as observed by scanning electron microscopy (SEM, Fig. 1b). These LSCF membranes were then coated with Al_2O_3 layers of different thickness, typically between 1 and 100 nm, by using ALD (Fig. S1). The room temperature XRD patterns of the coated samples are shown in Fig. S2 and indicates that only perovskite peaks are visible. A cross-section of the coating-membrane interface was then extracted in the form of a lamella by focused ion beam (FIB, Fig. S3) and examined by transmission electron microscopy (TEM) and energy dispersive X-ray analysis (EDX). The results, shown in Fig. 1c, indicate that as expected for typical ALD processes, the film is seemingly continuous and conformal on the surface of the membrane. This indicates that the coating is expected to protect the membrane against poisoning but also to limit the O_2 transport across it since the O_2 diffusivity of Al_2O_3 is 5 orders of magnitude lower than that of the LSCF [12]. The EDX analysis also indicates that there is no sign of chemical interaction or ion exchange between the coating and the membrane at this stage (Fig. 1c and Fig. S4). Moreover, the coating generally appears to be in amorphous, partially crystallized state, as revealed by the TEM micrograph detail shown in Fig. 1d.

3.2. The effect of coating thickness on O_2 permeation under H_2S

To investigate the impact of the coating on the O_2 transport properties, as well as its ability to alleviate H_2S poisoning, we prepared membranes having different coating thickness (Fig. 2a). Fig. 2b shows the O_2 permeation flux as a function of time, before, during and after H_2S exposure, for a membrane with no coating as well as for membranes coated with 30 and 100 nm Al_2O_3 layers. This plot shows that the uncoated membrane displays the highest initial O_2 permeation flux, decreasing by 15% and 85%, when 30 and 100 nm Al_2O_3 layers are employed, respectively. The O_2 permeation fluxes through membranes with a range of coating thicknesses are plotted in Fig. 2c. This plot indicates that for a coating thickness of up to about 20 nm, there is minimal negative impact on the O_2 transport capabilities of the LSCF membrane. For coatings of about 30 nm, a slight decrease in O_2 permeation is observed, as noted above, with permeation rapidly dropping as coatings approach the 100 nm thickness mark.

Upon introducing H_2S, the membranes display a marked decrease in O_2 permeation flux, as shown in Fig. 2b. That said all membranes appear to retain the perovskite phase after poisoning (Fig. S2). The uncoated membrane shows the largest drop, by about 95% of the initial O_2 permeation flux. The sudden drop in O_2 permeation is usually thought to be due to the blocking of surface oxygen vacancies by adsorbed poisoning species, e.g. H_2S [8,13,14]. Coated membranes appear to be more resilient, dropping by about 70% and 20% of the initial flux, for 30 and 100 nm coatings, respectively. This indicates that the Al_2O_3 coatings can limit the poisoning effect of H_2S to some degree, at the expense of lowering the initial O_2 permeation flux, as discussed above. Indeed, Fig. 2c shows that there seems to be an optimum coating thickness at around 30 nm, which provides the highest value of O_2 permeation flux under H_2S operation.

When H_2S is removed from the inlet stream, all membranes display a relatively fast recovery (possibly due to the unblocking of surface oxygen vacancies by desorption of poisoning species [8]), albeit not up to the initial O_2 permeation flux values. Flux recovery values (%) for a range of coating thickness are show in Fig. 2c. This plot indicates that for coatings thinner than 20 nm, flux recovery is low, resembling an uncoated membrane and thus presents no real benefit to alleviating H_2S poisoning. At the opposite side of the spectrum, 100 nm thick coatings show close to full recovery but their initial O_2 permeation flux values are too low to be of practical interest. Therefore, there seems to be an optimum coating thickness of about 30 nm, which balances a reasonable decrease in overall O_2 permeation flux values while providing reasonable protection during H_2S exposure and considerable flux recovery after exposure to H_2S.

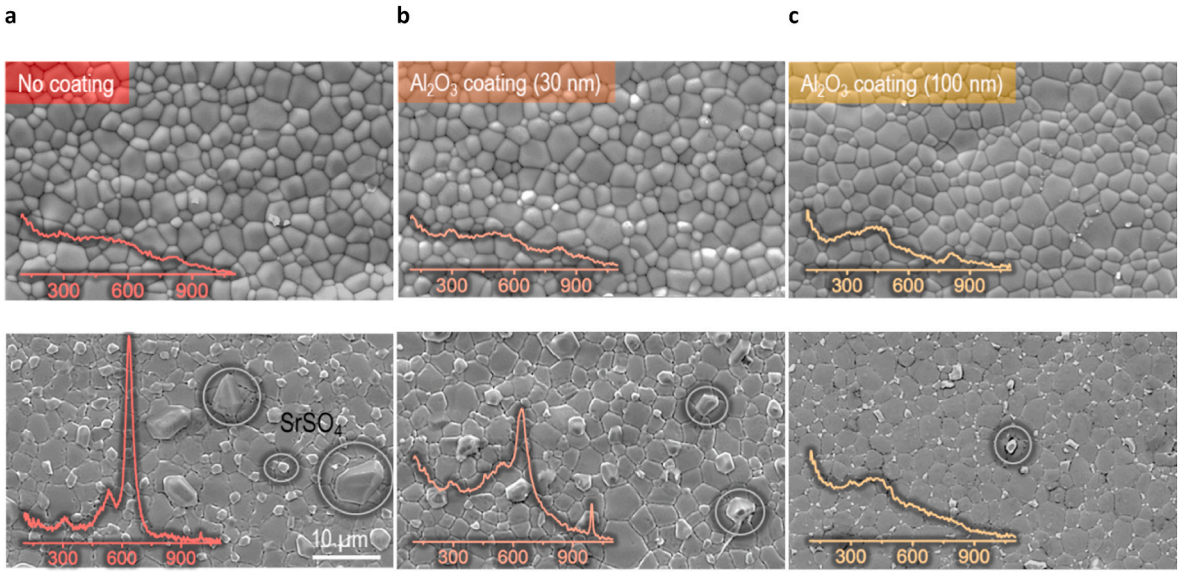

Fig. 3. Membrane surface morphology changes after O_2 permeation under H_2S. SEM micrographs and corresponding Raman spectra (x axis in cm^{-1}, y axis in a.u.) of membranes with: **(a)** no **(b)** 30 nm and **(c)** 100 nm coating. The upper images correspond with before exposure, lower images after exposure, to H_2S. The grey circles highlight $SrSO_4$ particle grown at the surface of the membrane.

3.3. Structural changes in the coated membranes after O_2 permeation under H_2S

To better understand the irreversible degradation of the O_2 permeation flux after exposure to H_2S, we compare the surface microstructure of representative membranes before and after the permeation experiments, as shown in Fig. 3. This figure shows that the surface morphology of the membranes with no coating and 30 and 100 nm coatings are initially very similar. The corresponding Raman spectra also confirms that, displaying a featureless spectrum, as expected for LSCF [15]. The SEM micrographs collected after the O_2 permeation experiments under H_2S reveal the formation of particles, as highlighted by grey circles in Fig. 3. According to the corresponding Raman spectra, these can be attributed to $SrSO_4$, based on the peaks at 458, 625 and 998 cm^{-1} [16, 17]. This indicates that Sr ions are being extracted from the perovskite lattice to form these particles. Moreover, since the coatings appear to be continuous and conformal on the membrane surface (Fig. 1c), Sr is being transported across the coating to form these particles. It is worth noting that the dimensions and occurrence of these particles decrease dramatically from the uncoated to the 30 nm coated membrane and further to the 100 nm coated membrane. This clearly illustrates the effectiveness of the coatings in limiting the formation of $SrSO_4$ particles,

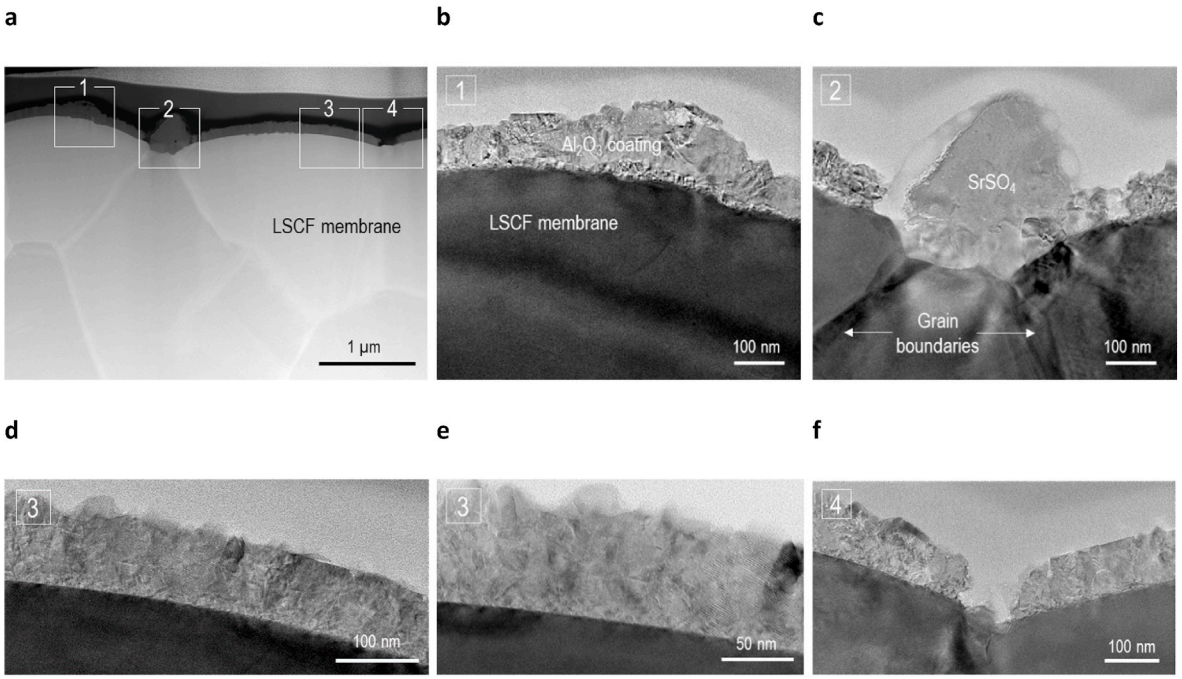

Fig. 4. Coating morphology changes after O_2 permeation under H_2S. TEM micrographs of the membrane-coating cross-section at various points of interest: **(a)** overview, highlighting local areas of interest; **(b)** in a region away from a perovskite grain boundary; **(c)** in the vicinity of perovskite grain boundaries; **(d)–(e)** details from **b** showing the polycrystalline nature of the coating; **(f)** in the vicinity of perovskite grain boundary absent of $SrSO_4$ particle.

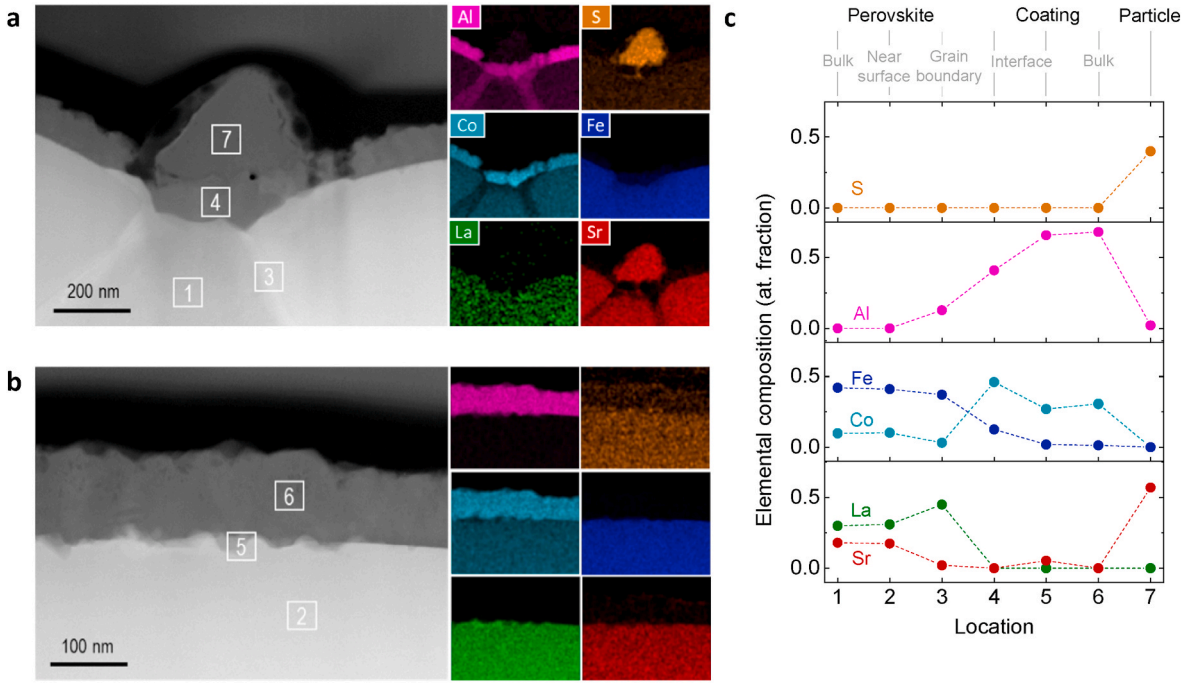

Fig. 5. Cation exchange between the membrane and the coating after O_2 permeation under H_2S. (a) TEM micrograph around a $SrSO_4$ and perovskite grain boundaries together with corresponding elemental maps obtained by EDX analysis. **(b)** TEM micrograph around the membrane-coating interface away from perovskite grain boundaries with corresponding elemental maps obtained by EDX analysis. **(c)** Elemental composition (normalized to 1) at different point locations marked on the micrographs shown in **a** and **b**. The dash lines serve as guide to the eye. The errors are smaller than the points.

and thus limiting Sr diffusion across it, although, as shown above, the coatings also limit O_2 permeation.

Insight into the membrane behaviour can be obtained by comparing the microscopy data in Fig. 3 to the permeation data from Fig. 2. The uncoated sample exhibits the highest initial values of O_2 transport and lowest under H_2S, coupled with the most extensive $SrSO_4$ growth and the lowest value of flux recovery after H_2S exposure. Since O^{2-} transport is required for O_2 permeation and both O^{2-} and Sr^{2+} ions are required $SrSO_4$ formation, this implies that in this sample both O^{2-} and Sr^{2+} ion mobilities are relatively high. On the contrary, for the 100 nm coated sample, the transport of both ions seems to be significantly inhibited, since this displays very limited $SrSO_4$ growth but also the lowest overall O_2 permeation flux. The 30 nm coated sample appears to be effective at selectively blocking Sr^{2+} diffusion more so than O^{2-} diffusion since this sample displays average $SrSO_4$ particle growth but still reasonably high O_2 permeation flux.

Close examination of the SEM micrographs after degradation in H_2S indicates that the $SrSO_4$ particles form almost exclusively at the grain boundaries. This is not surprising considering that there is ample evidence in the literature that for perovskites in particular, grain boundaries act as fast ion diffusion pathways for both oxide ions or cations [18–20]. The fact that the $SrSO_4$ particles grow at the grain boundaries is certainly consistent with this observation. At the same time, the irreversible degradation component of the O_2 permeation flux seems to also be linked to this. Indeed, the irreversible change to the grain boundary structure (and composition, see below), brought about by the formation of the $SrSO_4$ particles, appear to significantly decrease the degree of flux recovery, implying that a significant fraction of the oxygen transport was occurring through the grain boundaries of the membrane. Indeed, this is not surprising since grain boundaries ensure percolation between grains throughout the entire thickness of the membrane. Any change in ion conductivity of the grain boundaries is reflected in diminished transport across the membrane itself.

To further understand and characterize the structural changes occurring at the membrane-coating interface after O_2 permeation under H_2S, we extract electron-transparent lamellae of this interface and examine them by TEM, as shown in Fig. 4. We highlight various areas of interest, in the proximity and away from a perovskite grain boundary. Close-up TEM micrographs of the coating (Fig. 4b–f) illustrate that the coating has evolved to a highly polycrystalline state, whereas initially it was largely amorphous. The polycrystalline nature might facilitate O2-transport through it via grain boundaries, much like in the perovskite membrane, therefore allowing a degree of oxygen transport, which should otherwise not be possible for dense, single crystal Al_2O_3 [12]. The coating still appears to be conformal with respect to the membrane although it appears to be disrupted at the perovskite grain boundaries probably due to the formation of the $SrSO_4$ particles, as discussed above. Indeed, Fig. 4c shows a cross-section detail of such a particle.

3.4. Compositional changes in the coated membranes after O_2 permeation under H_2S

The microstructural evidence presented so far clearly indicates that the there is considerable ion transport across the coating, in order to ensure O_2 transport, as well as $SrSO_4$ formation. In order to better understand these transport processes and their consequence on membrane-coating composition, we carry out elemental mapping across this interface, in the proximity to, and also at a distance from, perovskite grain boundaries. The elemental maps are included in Fig. 5a and b, while the elemental composition (expressed as atomic fraction) at various points of interest marked with numbers is plotted in Fig. 5c. These data indicate that the bulk of the perovskite in the vicinity of the grain boundary and that of the film display similar compositions, equivalent to the nominal perovskite composition and therefore they were not affected by segregation processes. On the contrary, the grain boundary region of about 50–100 nm width experienced drastic compositional changes, being severely depleted of Sr ions (seemingly moving across the coating to form $SrSO_4$). It is enriched in La ions (probably to ensure charge neutrality in absence of Sr ions), it is Co depleted (which seemingly diffuses into the coating), and containing a

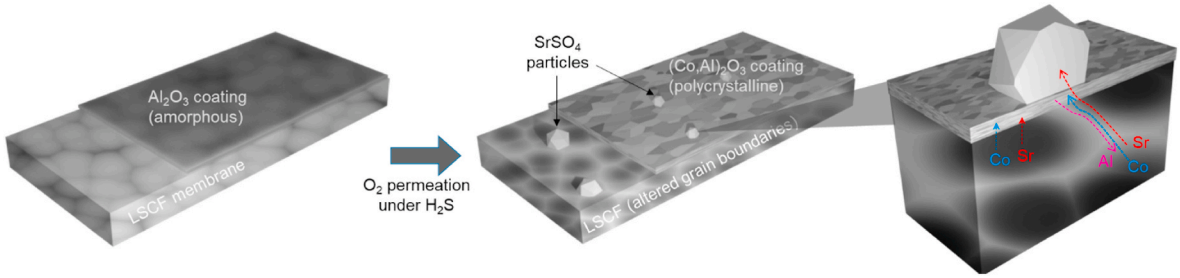

Fig. 6. Schematic evolution of coated membranes after O_2 permeation under H_2S. Initially the polycrystalline LSCF membrane is covered with an amorphous layer of Al_2O_3. After O_2 permeation under H_2S, the coating becomes polycrystalline and enriched with Co originating from the near surface region and grain boundaries of the LSCF membrane. Additionally, $SrSO_4$ grow at the surface grain boundary region of the perovskite; thicker coatings are more effective in limiting their growth.

large fraction of Al (coming from the coating).

This ion exchange is expected to have profound impact on the transport processes across the membrane. In particular, the depletion of Co (known to promote O^{2-} diffusion in perovskites) and enrichment of Al (which impairs O^{2-} diffusion) will mean that compositionally, the grain boundaries will be significantly less suitable for promoting O_2 transport [21,22]. Therefore, it seems that irreversible loss of O_2 permeation flux observed after H_2S exposure is not necessarily due to $SrSO_4$ particle formation on the grain boundaries. This may also be due to chemical changes in the grain boundaries (caused indirectly by particle growth), which are responsible for maintaining percolation and transport between perovskite grains and therefore across the membrane [23]. On the contrary, the fact that the Al_2O_3 coating becomes doped with Co is expected to enhance its O_2 permeation properties, which explains why a sufficiently thin (~30 nm) coating will limit Sr diffusion but allow O_2 transport across with negligible losses [22]. The chemical interactions between the membrane and the coating and the subsequent changes in membrane grain boundaries and surface morphology are schematically illustrated in Fig. 6.

4. Conclusions

In this work, we investigated the effect of Al_2O_3 coatings on LSCF membranes with respect to O_2 transport properties and protection against H_2S poisoning. We show that even though Al_2O_3 is not a good oxide ion conductor, sufficiently thin coatings of ~30 nm still allow high O_2 permeation fluxes, while providing protection against Sr segregation and subsequent H_2S poisoning. Following O_2 permeation, some ion exchange between the perovskite and the Al_2O_3 coating occurs (predominantly Co doping the coating), which also seems to contribute towards enhancing O_2 permeation across the coating. Coatings thinner than 30 nm do not appear to provide protection against poisoning, while coatings thicker than this value display even better stability but at the expense of dramatically decreased oxygen permeation fluxes. Moreover, we have shown that the irreversible loss of O_2 permeation flux following H_2S exposure is not necessarily directly due to the formation of surface $SrSO_4$, which would impair O_2 exchange and transport, but could be due to more subtle chemical changes that their formation triggers in the underlying structure of the grain boundaries of the membrane.

Declaration of competing interest

The authors declare that they have no known competing financial interests or personal relationships that could have appeared to influence the work reported in this paper.

Acknowledgements

The research leading to these results has received funding from the European Research Council under the European Union's Seventh Framework Program (FP/2007–2013)/ERC Grant Agreement Number 320725 and from the EPSRC via Grant EP/M01486X/1, EP/P007767/1, EP/P009050/1.

Data supporting this publication is available under a Creative Commons Attribution 4.0 International license, see 10.25405/data.ncl.11971641.

Appendix A. Supplementary data

Supplementary data to this article can be found online at https://doi.org/10.1016/j.memsci.2020.118736.

References

[1] J. Sunarso, S. Baumann, J.M. Serra, W.A. Meulenberg, S. Liu, Y.S. Lin, J.C. Diniz da Costa, Mixed ionic–electronic conducting (MIEC) ceramic-based membranes for oxygen separation, J. Membr. Sci. 320 (2008) 13–41, https://doi.org/10.1016/j.memsci.2008.03.074.

[2] X. Dong, W. Jin, N. Xu, K. Li, Dense ceramic catalytic membranes and membrane reactors for energy and environmental applications, Chem. Commun. 47 (2011) 10886–10902, https://doi.org/10.1039/C1CC13001C.

[3] A. Thursfield, A. Murugan, R. Franca, I.S. Metcalfe, Chemical looping and oxygen permeable ceramic membranes for hydrogen production – a review, Energy Environ. Sci. 5 (2012) 7421–7459, https://doi.org/10.1039/C2EE03470K.

[4] J. Xie, Y.-W. Ju, T. Ishihara, Influence of sulfur impurities on the stability of La0.6Sr0.4Co0.2Fe0.8O3 cathode for solid oxide fuel cells, Solid State Ionics 249–250 (2013) 177–183, https://doi.org/10.1016/j.ssi.2013.08.005.

[5] Y. Wei, W. Yang, J. Caro, H. Wang, Dense ceramic oxygen permeable membranes and catalytic membrane reactors, Chem. Eng. J. 220 (2013) 185–203, https://doi.org/10.1016/j.cej.2013.01.048.

[6] Y. Alqaheem, A. Thursfield, G. Zhang, I.S. Metcalfe, The impact of sulfur contamination on the performance of La0.6Sr0.4Co0.2Fe0.8O3−δ oxygen transport membranes,, Solid State Ionics 262 (2014) 262–265, https://doi.org/10.1016/j.ssi.2014.01.011.

[7] J. Gao, L. Li, Z. Yin, J. Zhang, S. Lu, X. Tan, Poisoning effect of SO2 on the oxygen permeation behavior of La0.6Sr0.4Co0.2Fe0.8O3−δ perovskite hollow fiber membranes, J. Membr. Sci. 455 (2014) 341–348, https://doi.org/10.1016/j.memsci.2013.12.073.

[8] P. Boldrin, E. Ruiz-Trejo, J. Mermelstein, J.M. Bermúdez Menéndez, T. Ramírez Reina, N.P. Brandon, Strategies for carbon and sulfur tolerant solid oxide fuel cell materials, incorporating lessons from heterogeneous catalysis, Chem. Rev. 116 (2016) 13633–13684, https://doi.org/10.1021/acs.chemrev.6b00284.

[9] C.C. Wang, K. Chen, S.P. Jiang, Sulfur deposition and poisoning of La0.6Sr0.4Co0.2Fe0.8O3-δ cathode materials of solid oxide fuel cells, J. Electrochem. Soc. 161 (2014) F1133–F1139, https://doi.org/10.1149/2.0041412jes.

[10] E. Granneman, P. Fischer, D. Pierreux, H. Terhorst, P. Zagwijn, Batch ALD: characteristics, comparison with single wafer ALD, and examples, Surf. Coating. Technol. 201 (2007) 8899–8907, https://doi.org/10.1016/j.surfcoat.2007.05.009.

[11] C. Endler-Schuck, J. Joos, C. Niedrig, A. Weber, E. Ivers-Tiffée, The chemical oxygen surface exchange and bulk diffusion coefficient determined by impedance spectroscopy of porous La0.58Sr0.4Co0.2Fe0.8O3−δ (LSCF) cathodes,, Solid State Ionics 269 (2015) 67–79, https://doi.org/10.1016/j.ssi.2014.11.018.

[12] A.H. Heuer, Oxygen and aluminum diffusion in α-Al2O3: how much do we really understand? J. Eur. Ceram. Soc. 28 (2008) 1495–1507, https://doi.org/10.1016/j.jeurceramsoc.2007.12.020.

[13] Y.-L. Huang, A.M. Hussain, C. Pellegrinelli, C. Xiong, E.D. Wachsman, Chromium poisoning effects on surface exchange kinetics of La0.6Sr0.4Co0.2Fe0.8O3−δ, ACS Appl. Mater. Interfaces 9 (2017) 16660–16668, https://doi.org/10.1021/acsami.7b02762.

[14] N. Ni, S.J. Cooper, R. Williams, N. Kemen, D.W. McComb, S.J. Skinner, Degradation of (La0.6Sr0.4)0.95(Co0.2Fe0.8)O3−δ solid oxide fuel cell cathodes at the nanometer scale and below, ACS Appl. Mater. Interfaces 8 (2016) 17360–17370, https://doi.org/10.1021/acsami.6b05290.

[15] L. Zhao, J. Zhang, T. Becker, S.P. Jiang, Raman spectroscopy study of chromium deposition on La0.6Sr0.4Co0.2Fe0.8O3-δ cathode of solid oxide fuel cells, J. Electrochem. Soc. 161 (2014), https://doi.org/10.1149/2.018406jes. F687.
[16] Y.-H. Chen, E. Huang, S.-C. Yu, High-pressure Raman study on the BaSO4–SrSO4 series, Solid State Commun. 149 (2009) 2050–2052, https://doi.org/10.1016/j.ssc.2009.08.023.
[17] W.P. Griffith, Raman studies on rock-forming minerals. Part II. Minerals containing MO3, MO4, and MO6 groups, J. Chem. Soc. A (1970) 286–291, https://doi.org/10.1039/J19700000286.
[18] S.P. Harvey, R.A.D. Souza, M. Martin, Diffusion of La and Mn in Ba0.5Sr0.5Co0.8Fe0.2O3−δ polycrystalline ceramics, Energy Environ. Sci. 5 (2012) 5803–5813, https://doi.org/10.1039/C1EE02740A.
[19] F. Chiabrera, I. Garbayo, L. López-Conesa, G. Martín, A. Ruiz-Caridad, M. Walls, L. Ruiz-González, A. Kordatos, M. Núñez, A. Morata, S. Estradé, A. Chroneos, F. Peiró, A. Tarancón, Engineering transport in manganites by tuning local nonstoichiometry in grain boundaries, Adv. Mater. 31 (2019), https://doi.org/10.1002/adma.201805360, 1805360.
[20] N.W. Kwak, S.J. Jeong, H.G. Seo, S. Lee, Y. Kim, J.K. Kim, P. Byeon, S.-Y. Chung, W. Jung, In situ synthesis of supported metal nanocatalysts through heterogeneous doping, Nat. Commun. 9 (2018) 4829, https://doi.org/10.1038/s41467-018-07050-y.
[21] D. Neagu, J.T.S. Irvine, 4.15-Perovskite Defect Chemistry as Exemplified by Strontium Titanate, in: second ed., in: J. Reedijk, K. Poeppelmeier (Eds.), Comprehensive inorganic chemistry II, Elsevier, Amsterdam, 2013, pp. 397–415, http://www.sciencedirect.com/science/article/pii/B9780080977744004216. (Accessed 29 July 2013).
[22] H. Iwahara, Ionic Conduction in Perovskite-type Compounds, in: T. Ishihara (Ed.), Perovskite Oxide for Solid Oxide Fuel Cells, Springer, 2009.
[23] H.J.M. Bouwmeester, A.J. Burggraaf, ChemInform abstract: dense ceramic membranes for oxygen separation, ChemInform 28 (1997), https://doi.org/10.1002/chin.199724298.